INTERNATIONAL JOURNAL FOR NUMERICAL METHODS IN ENGINEERING
Int. J. Numer. Meth. Engng 2007; **69**:2247–2263
Published online 15 August 2006 in Wiley InterScience (www.interscience.wiley.com). DOI: 10.1002/nme.1847

Numerical study of flow field induced by a locomotive fish in the moving meshes

Tony W. H. Sheu*, †, § and Y. H. Chen‡

Department of Engineering Science and Ocean Engineering, National Taiwan University, No. 1, Sec. 4, Roosevelt Road, Taipei 106, Taiwan, Republic of China

SUMMARY

In this paper, the equations of motion are solved together with the incompressible constraint condition to simulate the flow field induced by the two specified fish motions. Since the investigated flow/structure interaction varies with time, the analysis is conducted in the moving meshes. Within the arbitrary Lagrangian–Eulerian (ALE) framework, both the space conservation law and the geometric conservation law have been rigorously enforced on the discrete level. Grid points move along with the fish to facilitate the analysis of the induced flow field for revealing the interaction mechanism. The resulting wave and sinusoidal motions of the fish are addressed. Copyright © 2006 John Wiley & Sons, Ltd.

Received 21 September 2005; Revised 19 June 2006; Accepted 21 June 2006

KEY WORDS: flow/structure interaction; moving meshes; (ALE) framework; geometric conservation law; space conservation law; wave and sinusoidal motions

1. INTRODUCTION

The habitat of fish in water and its shape and moving mode have evolved to have an optimized situation. Scientists are, therefore, motivated to design a propelling system from the fish motion with improved efficiency. In 1960s and 1970s, Lighthill [1–4] and Wu [5–8] attempted to find an efficient three-dimensional fish-like swimming mode based on the slender body theory. More recently, the available whole-field velocimetry and numerical visualization have enabled us to make a detailed study of the flow field around the fish. For example, Anderson [9] and

*Correspondence to: Tony W. H. Sheu, Department of Engineering Science and Ocean Engineering, National Taiwan University, No. 1, Sec. 4, Roosevelt Road, Taipei 106, Taiwan, Republic of China.
†E-mail: twhsheu@ntu.edu.tw
‡E-mail: yenhaw@msn.com
§Professor.

Contract/grant sponsor: National Science Council; contract/grant number: NSC94-2611-E-002-021

Copyright © 2006 John Wiley & Sons, Ltd.

Wolfgang *et al.* [10, 11] illustrated the generation and the manipulation of vorticity in the swimming and turning fish. The mechanism for producing propulsive and transient force in oscillating flexible bodies and fins in water was experimentally and theoretically identified in the work of Triantafyllou *et al.* [12]. One can also refer to the review article [13] for an overview of the swimming mechanism for fish. In the literature, the effect of fluid viscosity and the influence of the surface force on the fish motion have been less explored. Gary [14] had presented a controversial argument that the drag applied on the swimming dolphin must be smaller than that obtained in towing the rigid dolphin by a large factor. This subject will be addressed in the present incompressible Navier–Stokes (NS) study. Based on the simulated results, we will compare the drag force induced by the moving and non-moving fish bodies.

The remainder of this paper is organized as follows. With moving meshes, the dimensionless working equations for the fluid flow are presented in Section 2. Within the semi-discretization framework, the resulting convection–diffusion–reaction (CDR) equations are obtained. In Section 3, the calculation of grid velocity is addressed so as to preserve the geometric conservation law. Validation of the CDR finite element model in moving meshes is given in Section 4. This is followed by the discussion of the simulated results. Finally, we present the concluding remarks.

2. WORKING EQUATIONS WITHIN ALE FRAMEWORK

The following incompressible Navier–Stokes equations are considered in the study of fish motion along with the viscous effect

$$\nabla \cdot \mathbf{u} = 0 \tag{1}$$

$$St\,\mathbf{u}_t + \mathbf{u} \cdot \nabla \mathbf{u} + \nabla p - \frac{1}{Re}\nabla^2 \mathbf{u} = \mathbf{f} \tag{2}$$

where St and Re denote the Strouhal number $St = L/TU$ and the Reynolds number $Re = \rho_f U L/\mu$. ρ_f/μ is the kinematic viscosity of the fluid and L and U are the user-specified characteristic length and velocity, respectively. The coupled momentum and continuity equations are solved in this study so that the mass conservation law is unconditionally satisfied. Since the simulated fish body is time-dependent, the girds are allowed to move with time to adopt the flow domain. Within the ALE framework, Equation (2) can be identically represented by

$$St\,\mathbf{u}_t + (\mathbf{u} - \mathbf{u}_g) \cdot \nabla \mathbf{u} + \nabla p - \frac{1}{Re}\nabla^2 \mathbf{u} = \mathbf{f} \tag{3}$$

In the above equation, calculation of the grid velocity $\mathbf{u}_g = St(\mathbf{r}_t)$ warrants a special care.

To describe the finite element model, the following transient convection–diffusion equation is considered:

$$\phi_t + \mathbf{u} \cdot \nabla \phi - \mu \nabla^2 \phi + R\phi = f \tag{4}$$

Our semi-discretization method starts with approximating ϕ_t by means of

$$\phi_t = \frac{\phi^{n+1} - \phi^n}{\Delta t} \tag{5}$$

Copyright © 2006 John Wiley & Sons, Ltd.

DOI: 10.1002/nme

The superscripts n and $n+1$ represent two consecutive times at t^n and t^{n+1}, with an incremental time step Δt ($\equiv t^{n+1} - t^n$). Substitution of Equation (5) into (4) yields the following implicit equation containing only the spatial derivative terms:

$$\mathbf{u} \cdot \nabla \phi^{n+1} - \mu \nabla^2 \phi^{n+1} + \left(R + \frac{1}{\Delta t} \right) \phi^{n+1} = f(x) + \frac{1}{\Delta t} \phi^n \tag{6}$$

The originally investigated transient convection–diffusion equation (4) is now transformed into the steady-state convection–diffusion–reaction (CDR) equation (6). We are, therefore, able to apply our previously developed convection–diffusion–reaction finite element model [15] to solve the transient transport equation (4).

3. GEOMETRIC CONSERVATION LAW AND GRID VELOCITY

The simulation of conservation equation (3) on the moving meshes requires the value of $\mathbf{u}_g$. On the continuous level, the space conservation law (SCL) and the volume conservation law (VCL) are naturally satisfied. The SCL implies that each cell should be closed by its surfaces, and the VCL states that the volume change of a moving cell must be equal to the sum of the volume increase along its surface that encloses the volume. The combination of the SCL and the VCL is the geometric conservation law (GCL) [16]. Equations (7) and (8) represent the SCL and the VCL, respectively [17],

$$\oint_B \mathbf{a} \cdot \mathrm{d}\mathbf{s} = 0 \tag{7}$$

$$\frac{\partial V}{\partial t} = \oint_B \overline{\mathbf{w}} \cdot \mathrm{d}\mathbf{s} = 0 \tag{8}$$

In the above equations, $\mathbf{s}$ represents the area vector with its direction normal to the boundary surface B of the time-varying volume V. $\mathbf{a}$ and $\overline{\mathbf{w}}$ represent the constant-velocity flow direction in any non-moving mesh and the specified boundary velocity vector for B, respectively. While Equations (7) and (8) are unconditionally satisfied in the continuous sense, they are not always satisfied in their discrete description. In the course of simulation, violation of the GCL will cause the prediction accuracy to deteriorate in two ways. The dissatisfaction of the SCL will lead to an erroneously calculated convection velocity and also the dissatisfaction of the discrete VCL will cause the mass to accumulate or diminish owing to the numerically introduced source and sink, respectively. While errors of these kinds have long been recognized, they were not seriously addressed in many previous reports.

The Galerkin finite element analysis in the moving meshes described in Equation (3) requires the value of $\mathbf{u}_g$. By integrating the GCL condition in its differential description and employing the divergence theorem, the GCL condition in its integral description is obtained as shown in Equation (8). In other words, the calculation of grid velocity is constrained by the following GCL condition:

$$\frac{1}{\sqrt{g}} \frac{\partial \sqrt{g}}{\partial t} = \nabla \cdot \mathbf{u}_g \tag{9}$$

Copyright © 2006 John Wiley & Sons, Ltd.

DOI: 10.1002/nme

The $\sqrt{g}$ shown above represents the determinant of the Jacobian matrix, which relates the fixed and the moving co-ordinates. The way to move nodes from their previous locations to the updated ones in each time step is as follows: We assume that (u_g, v_g) remains unchanged in magnitude as well as in direction from (x^{old}, y^{old}) to the updated location at (x^{new}, y^{new}). One way to satisfy the VCL and the SCL and, thus, the GCL is to calculate u_g and v_g by $u_g = (x^{new} - x^{old})/\Delta t$ and $v_g = (y^{new} - y^{old})/\Delta t$. The rigorous proof for this calculation is given in Chen and Sheu [18].

4. VALIDATION OF THE ALE FINITE ELEMENT CODE

To validate the current method, the 2D channel flow with a moving indentation is considered. This problem was numerically studied by Ralph and Pedley [19], Demirdzic and Peric [20], Lai and Przelwas [21], and experimentally investigated by Pedley and Stephanoff [22]. The indented wall schematic in Figure 1 is given by

$$y(x) = \begin{cases} h & \text{for } 0 < x < x_1 \\ 0.5h\{1 - \tanh[a(x - x_2)]\} & \text{for } x_1 < x < x_3 \\ 0 & \text{for } x > x_3 \end{cases} \tag{10}$$

where $a = 4.14$, $x_1 = 4$, $x_3 = 6.5$, $x_2 = 5.25$ and $h = \frac{1}{2}h_{max}[1 - \cos(2\pi t)]$ with $h_{max} = 0.38$. The Reynolds number (Re) in the current study is 507 and the Strouhal number (St) is 0.037. Subjected to an initially fully-developed velocity, the simulation involves 16 000 elements and the time step Δt is chosen as 0.001. During the calculation, the inlet condition is kept unchanged and the zero gradient condition for the field variables is applied at the channel outlet.

Due to the cyclic motion of the indented wall, the vortices are generated and destroyed periodically. In Figure 2, three main vortices, namely, A, B and C are seen at $t = 0.6$. The locations of the crests and troughs for the eddies B and C are plotted in Figure 3. The dimensionless length X^* $(= x(10St)^{1/3})$ is proportional to $(St)^{1/3}$ and is independent of Re. In Figure 3, good agreement between the present results and the experimental observation [22] and other numerical results [21] is seen.

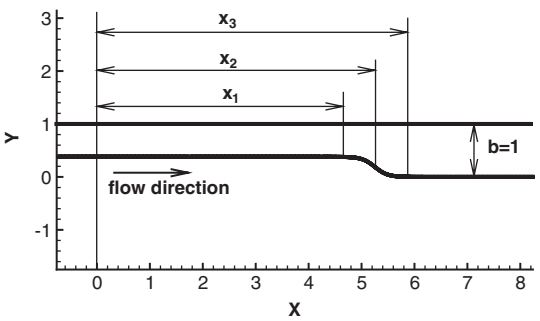

Figure 1. Schematic of the 2D channel with a moving indentation.

Copyright © 2006 John Wiley & Sons, Ltd.

DOI: 10.1002/nme

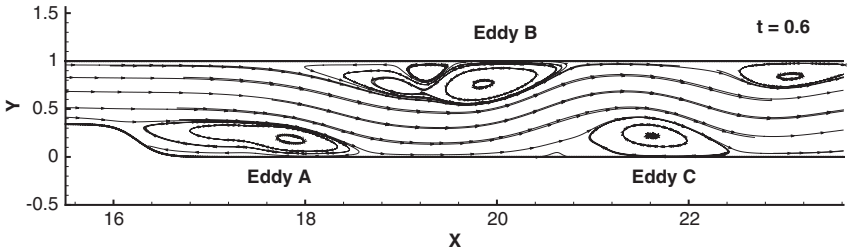

Figure 2. The simulated streamlines and vortices A, B, C at $t = 0.6$.

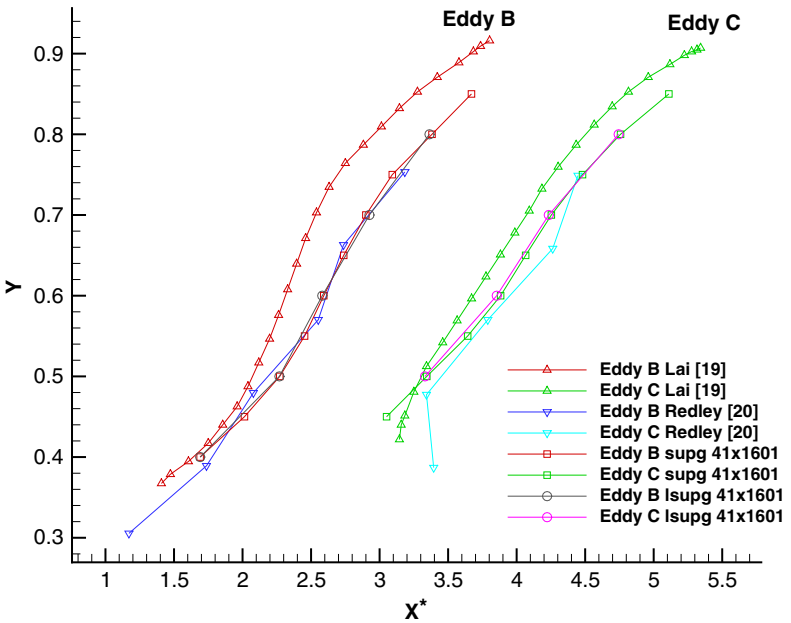

Figure 3. A comparison of positions of eddies B and C.

To validate the present numerical results, the mass conservation law must be satisfied, namely the local mass conservation (LMC) and the global mass conservation (GMC). The LMC and GMC are given by LMC $\equiv \int_{\Gamma_e} (\mathbf{u} \cdot \mathbf{n})\, \mathrm{d}s$ and

$$\mathrm{GMC} = \int_{\Gamma} (\mathbf{u} \cdot \mathbf{n})\, \mathrm{d}s = \sum \int_{\Gamma_e} (\mathbf{u} \cdot \mathbf{n})\, \mathrm{d}s \tag{11}$$

In Figure 4, the computed value of GMC is seen to lie between 7.91×10^{-13} and 4.174×10^{-16}. The mass conservation is well preserved even though the domain undergoes a larger deformation. In Figure 5, we plotted the region with a large value of LMC and pressure contours at $t = 1.5$. In this figure, the value of |LMC| at each point is represented by the size of the square. In other words, if the size of the square approaches zero, the mass conservation is preserved. Within the rectangular enclosures shown by the dashed lines, the local mass conservation is less satisfied near

Copyright © 2006 John Wiley & Sons, Ltd.

DOI: 10.1002/nme

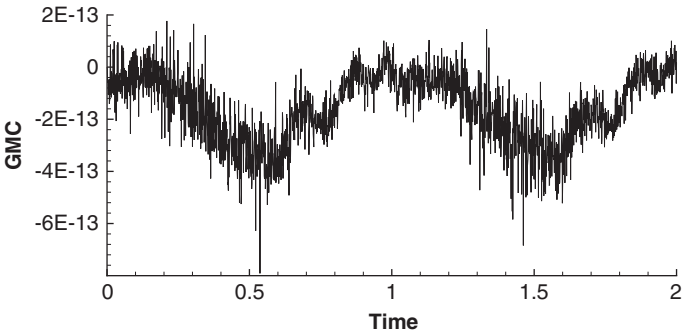

Figure 4. The simulated value of GMC against time.

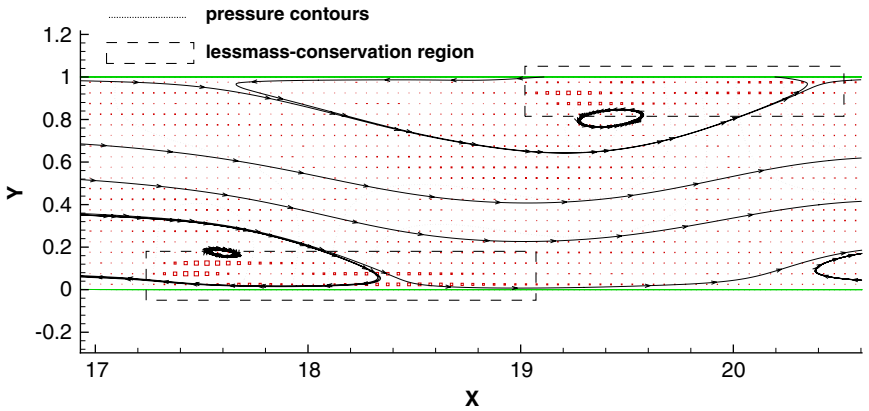

Figure 5. The distribution of LMC magnitudes in the region having a high pressure gradient.

the higher pressure gradient part. The value of |LMC| lies between 4.0×10^{-4} and 1.0×10^{-10}, instead of zero. From the above discussion, it can be concluded that the present finite element method fails to maintain the mass conservation exactly in the very high pressure gradient region. This result is not surprising in the sense that the use of finite element method satisfies the global mass conservation and the local mass conservation is not exactly maintained everywhere.

5. RESULTS AND DISCUSSION OF FISH-LIKE MOTIONS

In order to simplify the analysis, the chosen Robo Tuna fish is allowed to move only along the x direction. The fish model under the current investigation has a length of L and its body profile assumes the form given by [23, 24]

$$y_1(x) = \frac{y^*(x^*)}{L} = \pm 0.152 \tanh\left(\frac{6x^*}{L} + 1.8\right) \quad \text{for } -0.3 < \frac{x^*}{L} < 0.1 \tag{12}$$

Copyright © 2006 John Wiley & Sons, Ltd.

DOI: 10.1002/nme

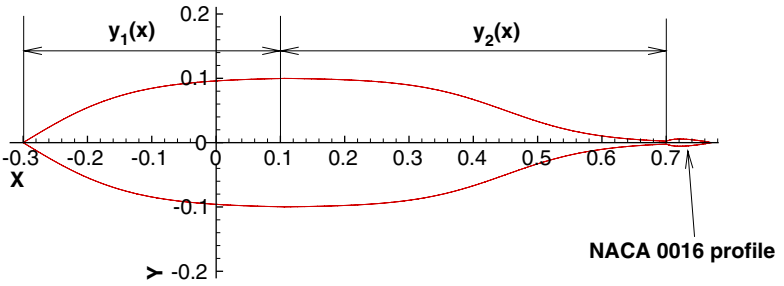

Figure 6. Schematic of the fish profile.

$$y_2(x) = \frac{y^*(x^*)}{L} = \pm\left(0.075 - 0.076\tanh\left(\frac{7x^*}{L} + 3.15\right)\right) \quad \text{for } 0.1 < \frac{x^*}{L} < 0.7 \tag{13}$$

The length of the NACA0016 caudal fin is $0.07L$. By virtue of Equations (12) and (13), the area of the investigated fish schematic in Figure 6 is calculated as $A = 2(\int_{-0.3}^{0.1} y_1(x)\,\mathrm{d}x + \int_{0.1}^{0.7} y_2(x)\,\mathrm{d}x) = 0.191611$. The cross section is assumed to be elliptical with a major to minor ratio ($AR = 1.5$), and hence the volume is given by $V = 4\pi AR(\int_{-0.3}^{0.1} y_1(x)^2\,\mathrm{d}x + \int_{0.1}^{0.7} y_2(x)^2\,\mathrm{d}x) = 0.222581$.

We consider that the fish backbone varies with time according to the following wave form [23]:

$$y_b^*(x^*, t^*) = a^*(x^*)\sin(k_w x^* - \overline{\omega} t^*) \tag{14}$$

where

$$a^*(x^*) = c_1 x^* + c_2 (x^*)^2 \tag{15}$$

In the above equations, K_w ($= 2\pi/\lambda^*$) denotes the wave number and $\overline{\omega}$ ($= 2\pi/T$) denotes the circular frequency. The dimensionless form of Equation (14) is as follows:

$$y_b(x, t) = a(x)\sin\left(\frac{2\pi}{\lambda}x - 2\pi t\right) \tag{16}$$

where the dimensionless wavelength is $\lambda = \lambda^* L$ and

$$a(x) = c_1 x + c_2 x^2 \tag{17}$$

The time t^* is replaced with tT and the period of waveform T is taken as the reference time. In the amplitude envelope $a(x)$, c_1 and c_2 are the two parameters used to generate different configurations. The point $x = 0$ is chosen at a distance of 30% of the fish length from its nose as shown in Figure 6. The motion of the fish backbone is plotted in Figure 7 for the case with $c_1 = 0.00232$, $c_2 = -0.163$ and $\lambda = 1.475$. In Figure 7, the fish shape is obtained by adding Equations (12) and (13) for the fish profile and Equation (14) for the backbone and is expressed as

$$y(x, t) = \begin{cases} y_b(x, t) \pm y_1(x, t) & \text{for } -0.3 < x < 0.1 \\ y_b(x, t) \pm y_2(x, t) & \text{for } 0.1 < x < 0.7 \end{cases} \tag{18}$$

Copyright © 2006 John Wiley & Sons, Ltd.

DOI: 10.1002/nme

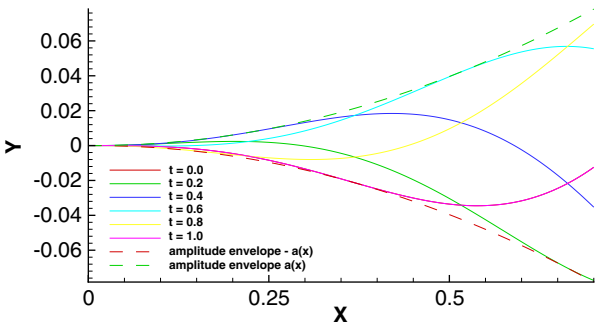

Figure 7. An illustration of the moving fish backbone.

In this simulation, the regeneration of grids is necessary for the up-and-down of the fish movement and is not necessary in the x direction.

To compute the velocity u_f and the displacement x_f of fish body, the following dimensionless equation of motion was employed.

$$St\,\frac{\mathrm{d}u_\mathrm{f}}{\mathrm{d}t} + 4\pi\xi S_\mathrm{n} u_\mathrm{f} + 4\pi^2 (S_\mathrm{n})^2 x_\mathrm{f} = \frac{F_i}{m} \tag{19}$$

where ξ is the damping coefficient and m $(=m^*/\rho_\mathrm{f} L^2)$ is the dimensionless mass. The dimensional mass per unit length, namely m^*, is rewritten in terms of the density ratio R_ρ $(=\rho_b/\rho_\mathrm{f})$ and the cross section area A as

$$m = \frac{m^*}{\rho_\mathrm{f} L^2} = \frac{\rho_b A}{\rho_\mathrm{f} L^2} = R_\rho \frac{A}{L^2} \tag{20}$$

In Equation (19), St $(=L/TU)$ is called the Strouhal number, where T is the reference time, and S_n is called the natural Strouhal number, which can be chosen arbitrarily. As the system natural frequency (f_n) is used to normalize the time, St turns out to be equal to S_n. The external force F_i can either be the drag force F_x or the lift force F_y, depending on the fish movement. By integrating the stress along the fish body and the interface boundary Γ, the force vector can be calculated according to

$$\mathbf{F} = (F_x \hat{\mathbf{i}},\, F_y \hat{\mathbf{j}}) = \int_\Gamma \tilde{\tau} \cdot \mathbf{n}\, \mathrm{d}s = \int_\Gamma (\tau_{xx} n_x + \tau_{xy} n_y)\, \mathrm{d}s \hat{\mathbf{i}} + \int_\Gamma (\tau_{xy} n_x + \tau_{yy} n_y)\, \mathrm{d}s\, \hat{\mathbf{j}}$$

The moment referenced to the mass centre $\bar{x}_i$ $(\equiv \int x_i\, \mathrm{d}A / \int \mathrm{d}A)$ is given by

$$\begin{aligned} \mathbf{M}_G = M_z \hat{\mathbf{k}} &= \int_\Gamma \mathbf{r}_\mathrm{g} \times (\tilde{\tau} \cdot \mathbf{n})\, \mathrm{d}s \\ &= \int_\Gamma [(r_\mathrm{g})_x (\tau_{xy} n_x + \tau_{yy} n_y) - (r_\mathrm{g})_y (\tau_{xx} n_x + \tau_{xy} n_y)]\, \mathrm{d}s \hat{\mathbf{k}} \end{aligned} \tag{21}$$

where $\mathbf{r}_\mathrm{g}$ is located between the boundary point and the mass centre.

Copyright © 2006 John Wiley & Sons, Ltd.

DOI: 10.1002/nme

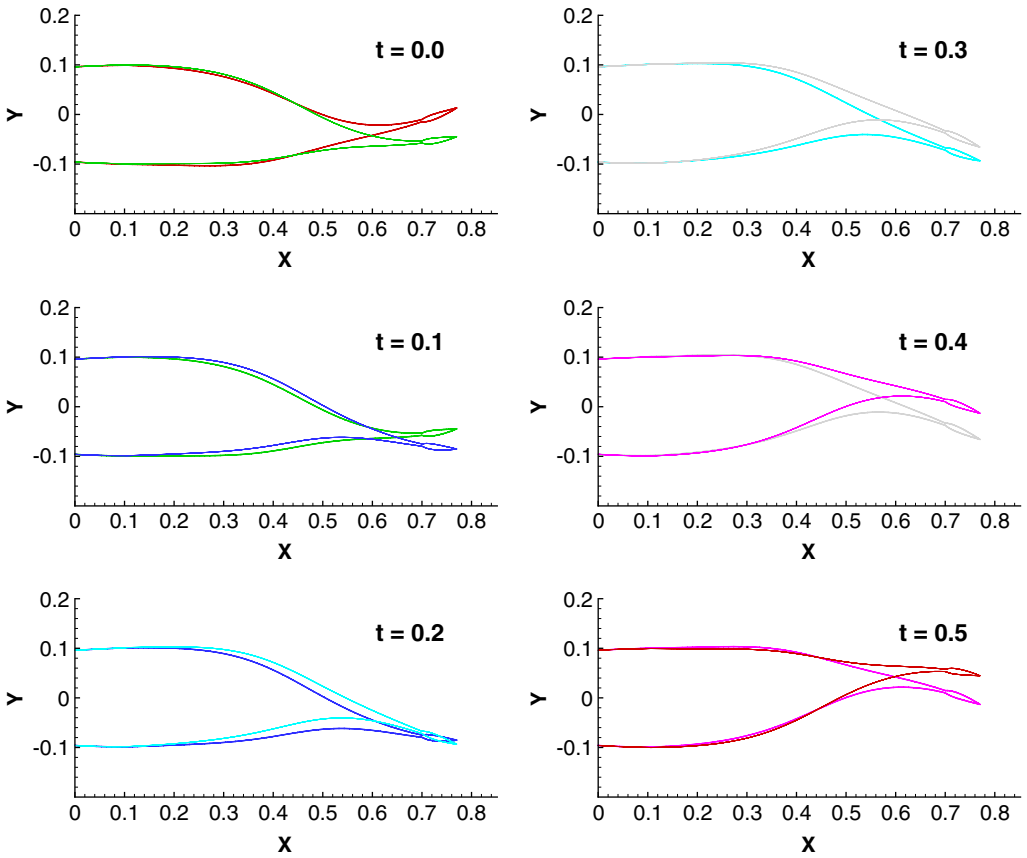

Figure 8. The switching of the caudal fin at different times.

The steps involved in the present simulation are described as follows: The fish shape Γ_f is determined first from Equation (18) to render Figure 8. This is followed by the grid generation to obtain the proper new solution points. Then the grid velocity is computed to solve the NS equations. By virtue of Equation (21), the stress along Γ_f is integrated to obtain the force applied on the fish body. Finally, the equation of motion (19) is solved to obtain the new fish velocity. The above procedures are repeated until the terminated time is reached.

In Figure 9, the gradient type boundary condition is specified at the free stream boundary Γ_o. The no-slip condition is applied on the fluid/solid interface and the boundary moving velocity is assigned as the flow velocity, $\mathbf{u}|_\Gamma = \mathbf{u}_g|_\Gamma$. In the simulation, 3120 elements and 12 830 nodal points are generated in the domain Ω, with more points clustered near the fish body. As the flow near the caudal fin is very complex, many vortices may be generated here and, hence, a fine mesh is generated at this caudal fin region. The length of the Tuna fish is taken as 1 m and its volume is 0.222 m^3. The density ratio of the fish and water is assumed as $R_\rho = (\rho_{\text{fish}}/\rho_{\text{water}}) = 1$.

As the fish swims forward with the velocity of -0.147, the streamlines are plotted in Figure 10 from $t = 4.0$–4.5 at $(St, Re) = (0.5, 2000)$. As the fish moves forward, two vortices are seen to be

Copyright © 2006 John Wiley & Sons, Ltd.

DOI: 10.1002/nme

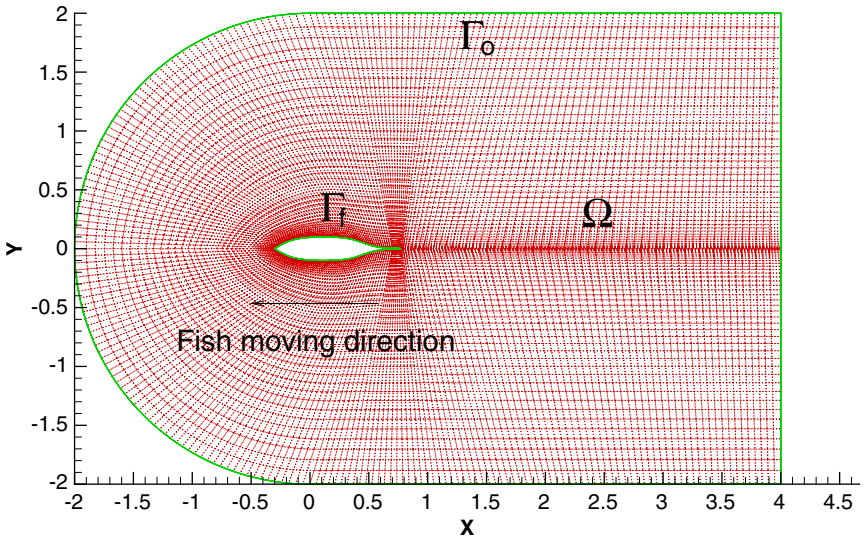

Figure 9. Schematic of the computational domain and its boundaries.

regularly generated at each side of the fish body. Their locations and sizes keep changing with the fish velocity. The fish position, the velocity and the drag force (F_x) applied on the fish are plotted in Figure 11 for $(St, Re) = (0.5, 2000)$. From the simulated displacement, it is observed that the specified backbone motion makes the fish to swim forward continuously (x-direction). The net force applied along the x-direction changes its sign alternately. As the absolute value of the negative force is larger than its positive counterpart, the fish can move along the negative x-direction due to the viscous effect. There are two types of force applied on the fish, known as the pressure force and the viscous force. In order to show their roles, F_x was separated into two parts. One force is contributed from the pressure $(F_x)_p$ and the other from the viscosity $(F_x)_v$. The F_x, $(F_x)_p$, $(F_x)_v$ and velocity at $t = 3.0$–5.0 are plotted in Figure 12. It is found that $(F_x)_p$ is always negative and is considered as the source of propulsion. The simulated profile $(F_x)_p$ enlightens that the fish wave motion can always lead to a net force that can cause the fish to move towards the side with a small amplitude.

The maximum force $(F_x)_p$ is seen to appear at $t = 4.27$ and the caudal fin has the largest displacement at side (b) as shown in Figure 13. Arrows 1 and 2 seen in Figure 13 indicate the moving direction of each part of the fish. The part A of the fish moves towards the direction of arrow 1. In the incompressible fluid flow, the pressure side (positive) and the suction side (negative) always appear in pair. The pressure side is denoted as side (a) and side (b) is regarded as the suction side. In this figure, the dashed line and shaded region denote the pressure distribution along the fish surface. The magnitudes of pressure at sides (a) and (b) are almost the same, but their signs are different. Usually, the pressure force at the pressure side will generate a force which is capable of pushing the fish forward, while the pressure force at the suction side will generate an opposite one. From this point of view, it is observed that if the fish locomotion is not proper, the force at one side may cancel that at the other side and the fish cannot move forward. By examining the side (a), it is noted that the pressure is positive. There exists an angle θ_a between the moving direction and the fish surface. The existence of this angle has caused the positive normal pressure

Copyright © 2006 John Wiley & Sons, Ltd.

DOI: 10.1002/nme

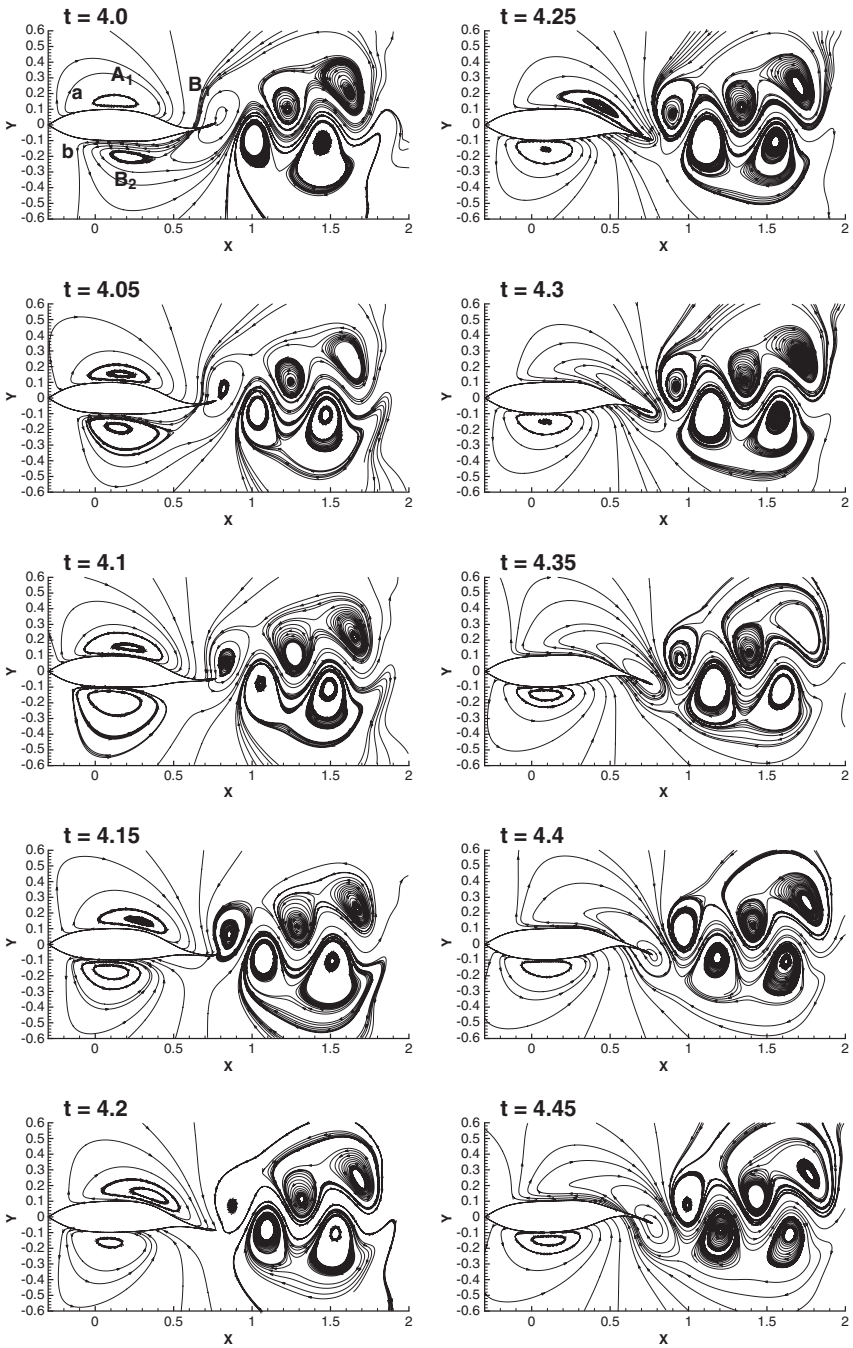

Figure 10. The simulated time-varying streamlines at $Re = 2000$ and $St = 0.6$.

Copyright © 2006 John Wiley & Sons, Ltd.

DOI: 10.1002/nme

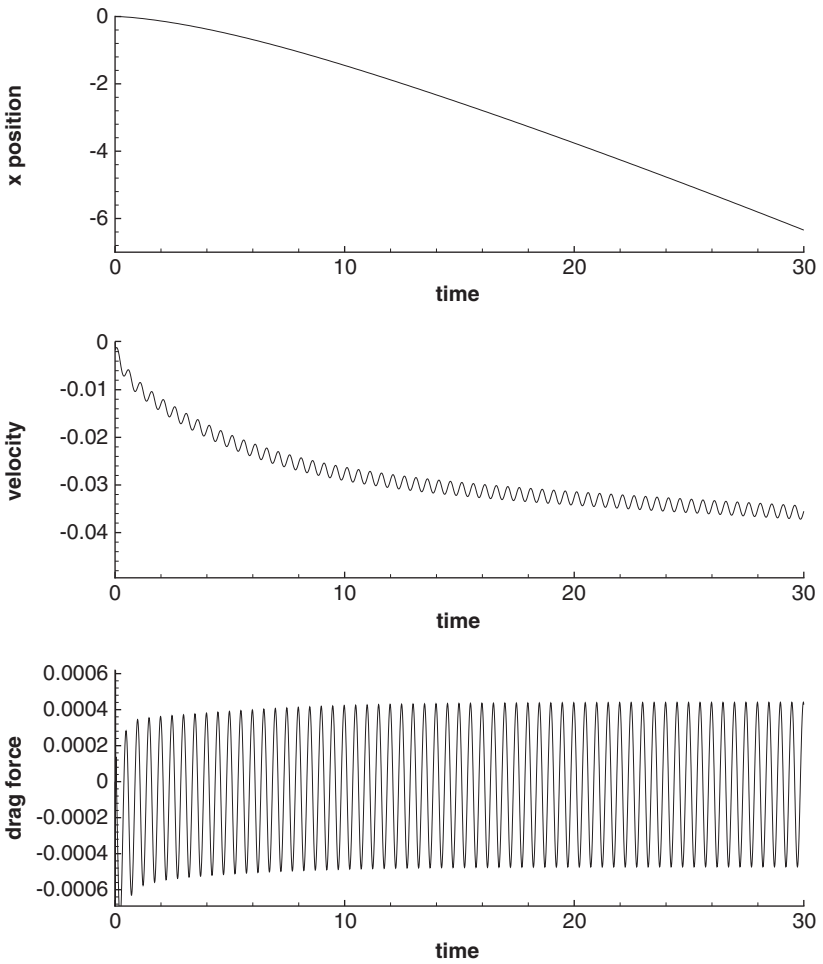

Figure 11. The simulated location, velocity and force F_x for the fish under investigation.

to distribute along the negative x-direction. At this moment, the side (b) is so adjusted that it is parallel to the moving direction. This can avoid the negative normal pressure force produced along this direction. In order to further support this argument, the pressure is integrated along each side of the fish body at different t. The force along the x-direction is plotted in Figure 14. When one side of the fish body has provided the maximum pushing force (point a) to make the fish to move forward, the shape at the other side is so adjusted to reduce the oppositive force to zero (point b).

From the previous discussion, it is noted that the force along the y-direction will be generated so that the z-direction moment cannot be avoided. The fish wave motion is featured with the presence of time-varying inflection point, which results in different parts of fish body to switch towards the opposite direction. The z-direction moment with opposite sign is generated from different parts. The switch of caudal fin can, thus, stabilize the fish body. Another part of the force applied on the fish is of the viscous type. The ratio $(F_x)_v/(F_x)_p$ is about -0.75 to -1.75. Both the viscosity

Copyright © 2006 John Wiley & Sons, Ltd.

DOI: 10.1002/nme

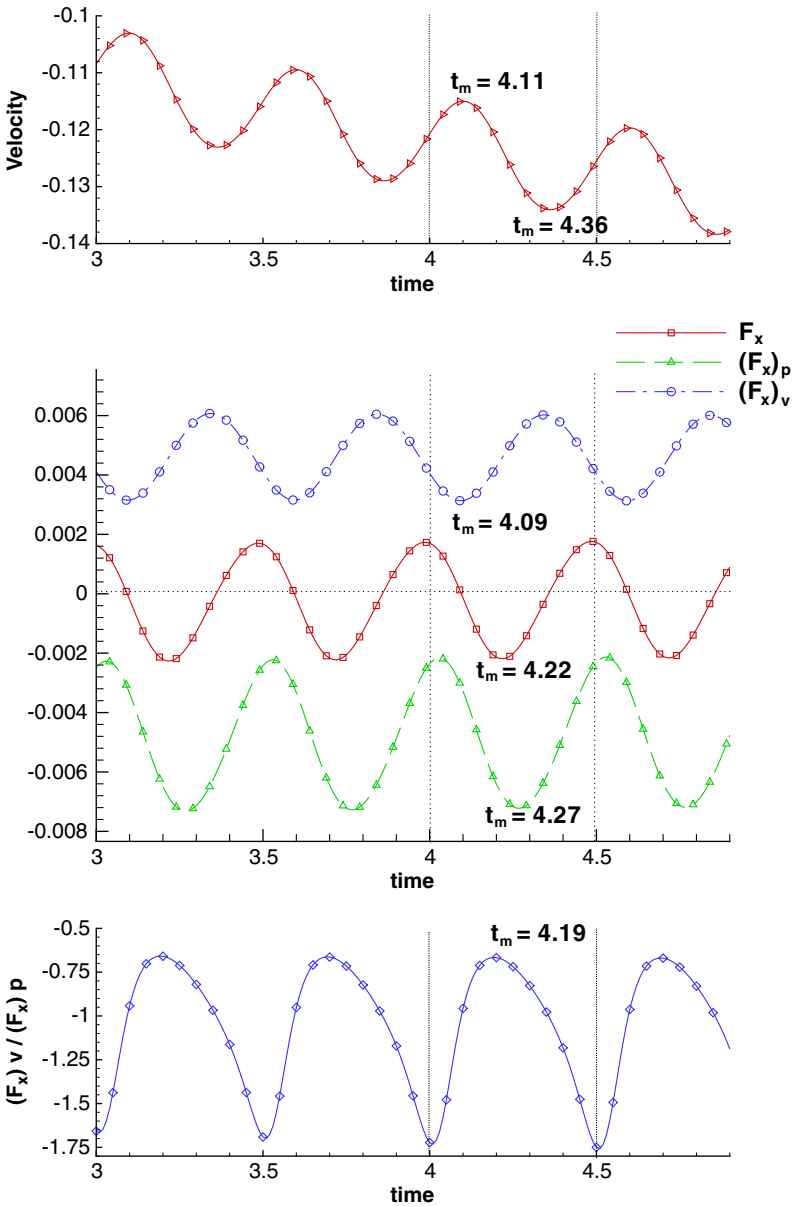

Figure 12. The simulated forces F_x, $(F_x)_p$, $(F_x)_v$ and the velocity for the investigated fish.

and the normal pressure are equally important. The $(F_x)_v$ is always positive since the viscous force direction is, by theory, opposite to the velocity direction. Thanks to this force the fish with the presently prescribed wave motion may be stopped in water. From this study, the fish with a wave-type motion can generate the force to make itself to move forward and also can stabilize the fish body. For a detailed study the form drags for both the moving and the stationary fish are

Copyright © 2006 John Wiley & Sons, Ltd.

DOI: 10.1002/nme

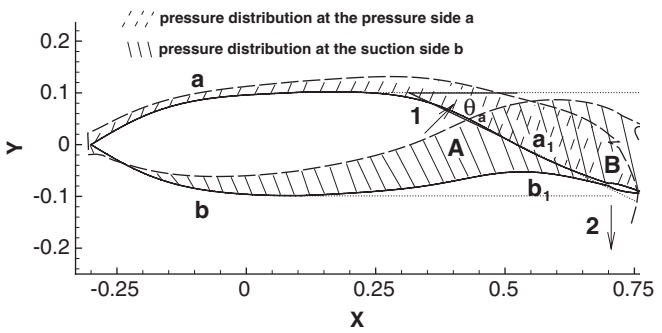

Figure 13. The simulated surface pressure force at $t = 4.25$.

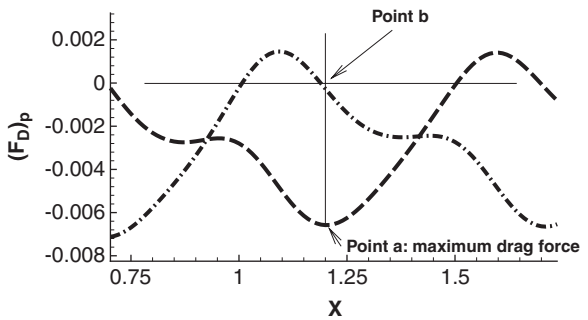

Figure 14. The simulated forces F_x on each side of the fish body.

calculated. The maximum form drag for the moving fish is about 0.002, while for the stationary fish is 0.0036. The maximum form drag of the moving fish is found to be smaller than that of the stationary fish and this difference is, however, negligible. Also the form drag of the moving fish does not remain constant. At a particular moment, the very large form drag ratio agrees with that obtained by Gray [14]. However, the conclusion made by Gray is proper only at one particular moment of the fish motion.

To validate the present results, the sinusoidal fish motion given below is also considered

$$y_b(x, t) = a(x) \sin(-2\pi t) \tag{22}$$

where

$$a(x) = c_1 x + c_2 x^2 \tag{23}$$

The time-varying fish locations are plotted in Figure 15. It is observed that the displacement of the wave-motion becomes smaller than that of the sinusoidal motion type. The wave motion performs better than the sinusoidal motion from the displacement viewpoint. In Figure 16, the maximum velocities for two investigated motions are found to be very close. The minimum velocity of the wave motion is, however, larger than that produced by the sinusoidal one. From this point of view, a fish swimming with the wave form outperforms the sinusoidal type.

Copyright © 2006 John Wiley & Sons, Ltd.

DOI: 10.1002/nme

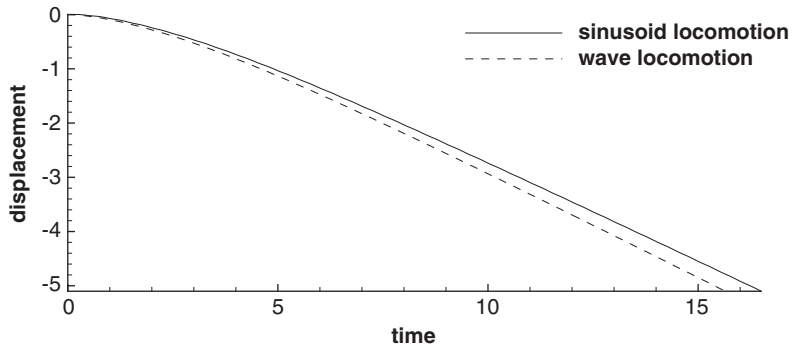

Figure 15. The time-varying displacement for the fish with the wave and the sinusoidal motions.

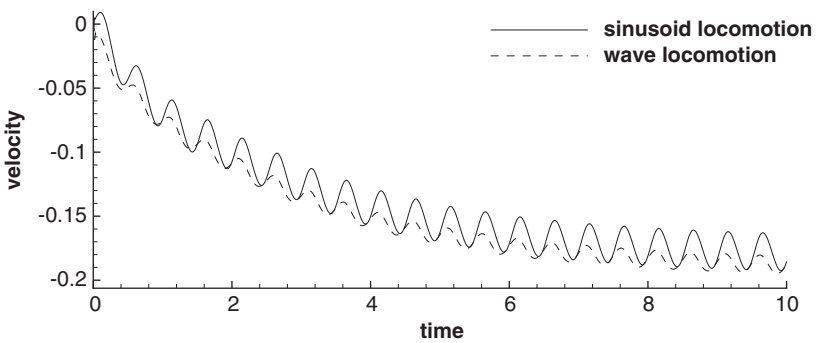

Figure 16. The time-varying velocity for the fish with the wave and the sinusoidal motions.

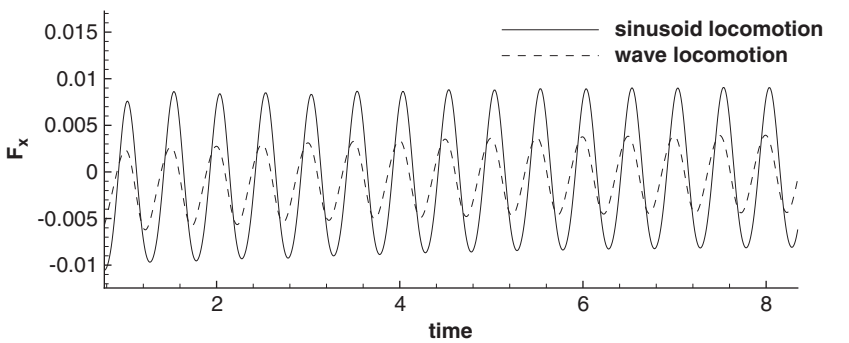

Figure 17. The time-varying force F_x for the fish with the wave and the sinusoidal motions.

From Figure 17, it is observed that F_x for the wave motion type is much smaller than that of the sinusoidal-motion type. The fish of a wave motion type is, thus, hydrodynamically more efficient than that with the sinusoidal motion. At the same swimming velocity, the fish with a wave motion uses only about 50% of the force. In Figure 18, the simulated F_y for the sinusoidal motion is

Copyright © 2006 John Wiley & Sons, Ltd.

DOI: 10.1002/nme

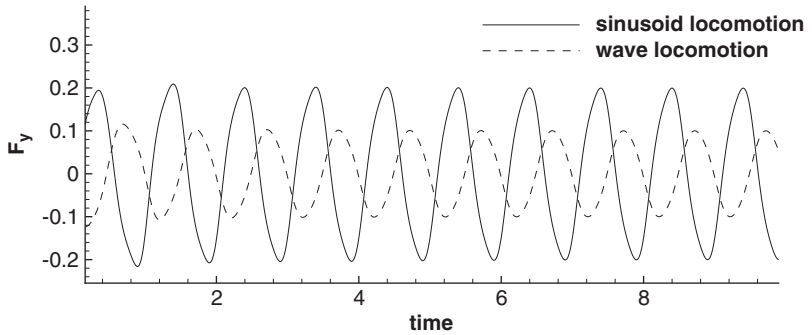

Figure 18. The time-varying force F_y for the fish with the wave and the sinusoidal motions.

larger than that of the wave motion. One character of the sinusoidal fish motion is that the moving part of the fish body moves in the same direction at a certain moment. As a result, the net force becomes larger. For the fish movement that is allowed only in the x direction, the one with a small F_y is found to be better, otherwise, F_y will induce a larger moment. The wave-fish motion is, therefore, more stable than the fish having a sinusoidal motion.

For the modelling of interaction between the fluid flow and the elastic fish body, the viscous flow equations are solved in the currently most available physical domain to render the pressure and stresses along the fish surface. With these simulated surface forces, the displacement vector for the elastic fish body can then be updated from the Navier equation, which governs the movement of the linearly elastic fish body with Young's modulus and Poisson ratio. The resulting predicted displacement enables us to update the configuration of flow domain, within which the flow equations are calculated in the new spatial domain. The above procedures are repeated over each time increment until the investigated fish shows a negligible change in its geometry. The reader can refer to [18] for additional details about the fluid–structure interaction solution algorithm.

6. CONCLUDING REMARKS

We have applied ALE finite element method to simulate the fish-like motion in the incompressible fluid flow at the fixed Reynolds and Strouhal numbers. The conclusion drawn from this study is that the fish can generate a net force that enables it to move forward. In addition, the fish with a wave-motion is hydrodynamically much better than the sinusoidal motion. While the amplitudes of the wave and sinusoidal motions are about the same, the displacement and velocity variation are quite different. The wave motion can result in not only a faster velocity but also a stable mechanism.

ACKNOWLEDGEMENTS

The support provided by the National Science Council under Grant NSC94-2611-E-002-021 is gratefully acknowledged.

Copyright © 2006 John Wiley & Sons, Ltd.

DOI: 10.1002/nme

REFERENCES

1. Lighthill M. Note on the swimming of slender fish. *Journal of Fluid Mechanics* 1960; **9**:305–317.
2. Lighthill M. Aquatic anmimal propulsion of high hydromechanical efficiency. *Journal of Fluid Mechanics* 1970; **44**:265–301.
3. Lighthill M. Large amplitude elongated-body theory of this locomotion. *Proceedings of the Royal Society of London B* 1971; **179**:125–138.
4. Lighthill M. *Mathematical Biofluid Dynamics*. Society for Industrial and Applied Mathematics: Philadelphia, 1975.
5. Wu T. Swimming of waving plate. *Journal of Fluid Mechanics* 1961; **10**:321–344.
6. Wu T. Hydromechanics of swimming propulsion. Part 1. Swimming of a two dimensional flexible plate at variable forward speeds in an inviscid fluid. *Journal of Fluid Mechanics* 1971; **46**:337–355.
7. Wu T. Hydromechanics of swimming propulsion. Part 2. Some optimum shape problems. *Journal of Fluid Mechanics* 1971; **46**:521–544.
8. Wu T. Hydromechanics of swimming propulsion. Part 3. Swimming and optimum movements of slender fish with side fins. *Journal of Fluid Mechanics* 1971; **46**:545–568.
9. Anderson JM. Vorticity control for efficient propulsion. *Doctoral Thesis*. Massachusetts Institute of Technology and the Woods Hole Oceanographic Institution, 1996.
10. Wolfgang M, Anderson JM, Grosenbaugh MA, Yue DKP, Triantafyllou MS. Near-body flow dynamics in swimming fish. *Journal of Experimental Biology* 1999; **202**:2303–2327.
11. Wolfgang M, Triantafyllou MS, Yue DKP. Visualization of complex near-body transport processes in flexible-body propulsion. *Journal of Visualization* 1999; **2**:143–151.
12. Triantafyllou MS, Triantafyllou GS, Yue DKP. Hydrodynamics of fishlike swimming. *Annual Review of Fluid Mechanics* 2000; **32**:33–53.
13. Sfakiotakis M, Lane DM, Davies JBC. Review of fish swimming modes for aquatic locomotion. *IEEE Journal of Oceanic Engineering* 1999; **24**(2):237–252.
14. Gray J. Studies in animal locomotion: VI. The propulsive powers of the dolphin. *Journal of Experimental Biology* 1936; **13**:192–199.
15. Sheu TWH, Chen YH. A multi-dimensional monotonic finite element model for solving the convection–diffusion–reaction equation. *International Journal for Numerical Methods in Fluids* 2002; **39**:639–656.
16. Thomas PD, Lombard CK. Geometric conservation law and its application to flow computations on moving grids. *AIAA Journal* 1979; **17**(10):1030–1037.
17. Zhang H, Reggio M, Trèpanier JY, Camarero R. Discrete form of the GCL for moving meshes and its implementation in CFD schemes. *Computers and Fluids* 1993; **22**(1):9–23.
18. Chen YH, Sheu TWH. Finite-element simulation of incompressible fluid flow in an elastic vessel. *International Journal for Numerical Methods in Fluids* 2003; **42**:131–146.
19. Ralph ME, Pedley TJ. Flow in a channel with a time-dependent indentation in one wall. *Journal of Biomechanical Engineering* 1990; **112**:468–475.
20. Demirdzic I, Peric M. Finite volume method for prediction of fluid flow in arbitrary shaped domains with moving boundaries. *International Journal for Numerical Methods in Fluids* 1990; **10**:771–790.
21. Lai YG, Przelwas A. A finite-volume method for fluid flow simulations with moving boundaries. *Journal of Computational Fluid Dynamics* 1994; **2**:19–40.
22. Pedley TJ, Stephanoff KD. Flow along a channel with a time-dependent indentation in one wall. *International Journal for Numerical Methods in Fluids* 1985; **160**:337–367.
23. Barrett DS. Propulsive efficiency of a flexible hull underwater vehicle. *Doctoral Thesis*. Massachusetts Institute of Technology, Cambridge, MA, 1996.
24. Barrett DS, Triantafyllou MS, Yue DKP, Grosenbaugh MA, Wolfgang M. Drag reduction in fish-like locomotion. *Journal of Fluid Mechanics* 1999; **392**:183–212.

Copyright © 2006 John Wiley & Sons, Ltd.

DOI: 10.1002/nme